Dear Reviewer:

We thank you for providing us the opportunity for explaining further the progress we have made. In the attached manuscript, we have

1. provided one section entitled ``Nonlinearity and Diverged trajectories,'' which includes numerical results of the 3D-NLM and calculations of the ensemble Lyapunov exponents with five additional figures (i.e., Figures 7-11);
2. provided Appendix A to discuss the derivations of Eq. (3) that includes the σY term;
3. provided Appendix B and Figure B1 to discuss the closed-form solution with elliptic functions and compare it with the closed-form solution represented by the elementary trigonometric functions in section 3;
4. provided Figure 5d to show the solutions near stable critical points (with different initial conditions for Xo) in the 3D-NLM with $r \neq 0$.

Our specific responses to your comments are provided below. We really appreciate your comments which have greatly improved the quality of the study and hope that our responses are acceptable.

Best Regards,

Dr. Bo-Wen Shen

Associate Professor
Department of Mathematics and Statistics
San Diego State University
5500 Campanile Drive
San Diego, CA 92182-7720
Tel: 619-594-5962
Email: bshen@mail.sdsu.edu

Responses to individual reviewers

Reviewer #1 (Comments to Author):
Review comments:

This is a well-written paper that deals with the so-called non-dissipative Lorenz model (NLM), which is 3D with X, Y and Z representing the amplitudes of selected Fourier modes. The system of equations describing the 3D-NLM has two nonlinear terms (XY and XZ) and one linear driving term rX, where r is the normalized heating parameter. Despite the fact that the system is called non-dissipative, one term with the Prandtl number is still present; I'd like to ask the author to comment in the paper on the presence and relevance of this term for the 3D-NLM. All terms of the 3D-NLM are the same as in the original 3D Lorenz model (3D-LM), however, the 3D-LM has two additional linear terms. In the studies presented in this paper, the author concentrates on the role played by the nonlinear terms and the linear heating term in the behavior of the 3D-NLM, and in its energy conservation.

Thanks for your valuable comments. We added Appendix A to discuss how we derived the 3D non-dissipative Lorenz model (3D-NLM) with the term σY retained. The term, σY, does not involve dissipative processes.

First, the author solves a nonlinear equation, which is obtained by elimination of Y and Z in terms of X, and by making an assumption that r = 0; with this assumption, the 3D-NLM is truly non-dissipative as the term with the Prandtl number disappears. He obtains the closed-form solutions, which represent wavelike (oscillatory) motions in phase space, and demonstrates that the nonlinear (X^2) term, called the nonlinear feedback loop, works together with the linear heating term to produce the resulting oscillatory solutions. This is a new and interesting result, which may be used to interpret solutions to the Duffing equation in the limit of no driving force and a small spring constant; there is an extensive literature about the Duffing system and its solutions, however, only very few papers deal with the above mentioned limits. I'd like to ask the author to comment in the paper on potential similarities and differences between the 3D-NLM and Duffing systems in the non-dissipative limits.

We added Appendix B to discuss how to reduce the Duffing equation into the equation $dX/d\tau + X^3/2=0$, which is investigated in this study, and then solve its solution in terms of elliptic functions. The solution is then inter-compared with the closed-form solution using elementary trigonometric functions in section 3 (as shown in Figure B1). They are in good agreement.

Since the 3D-NLM in the limit of r = 0 is non-dissipative (truly Hamiltonian), the author investigates its energy conservation and studies the resulting energy cycle. The studies of the latter are also extended to the cases when r is non-zero, which means that the term with the Prandtl number is included, and the formation of the so-called big cycle is observed. I'd like to suggest that the obtained results are also applied to the non-dissipative Duffing system and the resulting conclusions are included in the paper.

We discussed the characteristics of conservative systems with $r=0$ in section 3.2 and $r\neq0$ in section 3.3. The two systems are two special cases of Duffing equation, which is discussed in Appendix B in the revised manuscript.

Since the considered systems are Hamiltonian (or Hamiltonian-like) systems, it'd be interesting to explore the dependence of solutions on initial perturbations by using the KAM theorem, and the standard techniques, such as Lyapunov exponents, the Fast Lyapunov Indicator (FLI) and the Mean Exponential Growth Factor of Nearby Orbits (MEGNO) to investigate the onset of Hamiltonian chaos in these systems.

In the attached file, we added one section to discuss how the 3D-NLM can be analytically reduced to a 2D system and discuss the role of nonlinearity in producing diverged trajectories by analyzing the oscillatory solutions (i.e., Eqs. 26 and 27 in Figures 7 and 8) and performing the analysis of ensemble Lyapunov exponents (e.g., Figures 10 and 11).

In summary, this paper does contain new and significant results, which are presented clearly and concisely in the main text as well as in six figures. I'd like to recommend the paper for publication in NPG assuming that the author would address the above suggestions.

Thanks very much!

Manuscript prepared for Nonlin. Processes Geophys.
with version 2014/05/22 6.83 Copernicus papers of the LaTeX class copernicus.cls.
Date: 11 September 2014

On the nonlinear feedback loop and energy cycle of the non-dissipative Lorenz model

B.-W. Shen

Department of Mathematics and Statistics, San Diego State University, 5500 Campanile Drive, San Diego, CA, 92182, USA

Correspondence to: B.-W. Shen (bshen@mail.sdsu.edu; bowen.shen@gmail.com)

Abstract.

1 Introduction

This file provides responses to reviewers' comments. We thank the reviewers and Editor for providing us the opportunity for explaining further the progress we have made. In the manuscript, we have (1) provided one section entitled "Nonlinearity and Diverged trajectories", which includes numerical results of the 3D-NLM and calculations of the ensemble Lyapunov exponents with five additional figures (i.e., Figures 7-11); (2) provided Appendix A to discuss the derivations of Eq. (3) that includes the σ Y term; (3) provided Appendix B and Figure B1 to discuss the closed-form solution with elliptic functions and compare it with the closed-form solution represented by the elementary trigonometric functions in section 3; (4) provided Figure 5d to show the solutions near stable critical points (with different initial conditions for X_o) in the 3D-NLM with $r \neq 0$.

2 Nonlinearity and Diverged trajectories

Sensitive dependence of solutions on initial perturbations may also appear in conservative systems. This is called Hamiltonian chaos. To understand whether the 3D-NLM is chaotic or not, we first perform analytical analysis and then calculate and analyze ensemble Lyapunov exponents. As $dX/d\tau = \sigma Y$ in Eq. (3), Eq. (15) can be rewritten as: $dY/d\tau = -\frac{M^2}{\sigma}X$. The two equations with an initial condition $(X, Y) = (X_0, 0)$ lead to three critical points (X_c, Y_c) at $(0, 0)$ and ($\pm\sqrt{2\sigma r + X_0^2}$, 0). The first one $(0, 0)$ is unstable (as a saddle point), while the other two are stable. These critical points appear in association with the inclusion of the heating term, as the 3D-NLM with $r = 0$

only contains a trivial stable critical point at $(0,0)$. More importantly, the reduced system is two dimensional, and thus is not chaotic. In the following, we calculate the ensemble Lyapunov exponent (eLE) to check if and how it can reveal the stability of solutions in the 3D NLM assuming that we don't have prior knowledge of whether the system can be reduced to become two dimensional. [Through the processes, we may better understand the conditions under which the calculation of eLE may be applied to complicated weather and climate models.]

The Lyapunov exponent (LE) has been used to measure the average separation speed of nearby trajectories on the critical point (e.g., Froyland and Alfsen, 1984; Wolf et al., 1985; Nese, 1989; Zeng et al. 1991; Eckhardr and Yao, 1993; Christiansen and Rugh, 1997; Kazantsev 1999; Sprott, 2003; Ding and Li, 2007; Li and Ding, 2011). In Shen (2014a), the following two methods were implemented and tested: the trajectory separation (TS) method (e.g., Sprott, 2003) and the Gram-Schmidt reorthonormalization (GSR) procedure (e.g., Christiansen and Rugh, 1997). In this study, we only discuss the results from the second method. Calculations are conducted with a time interval ($\triangle\tau$) of 0.0001, and a total number of iterations, $N = 10,000,000$, yielding a total dimensionless time (τ) of 1,000. To minimize the dependence on the ICs, 10,000 ensemble (En=10,000) runs with the same model's parameters but different ICs are performed, and an ensemble-averaged LE is obtained from the average of the 10,000 LEs. Figure 7 shows the initial conditions for the ensemble runs, which represent white Gaussian noises. Figures 8a-c show the three LEs with $r = 0$ from the ensemble runs. The summation of the three LEs, shown in Fig. 8d, is very close to zero, suggesting that the system is conservative. The first leading LEs from the ensemble runs (Fig. 8a) show a Gaussian distribution with a mean of 0.004836 and median of 0.004853. With the long but still finite time period and the very large number ICs, the first ensemble LE (eLE) with a small but positive value may suggest the appearance of diverged trajectories.

The solutions in the 3D-NLM with $r \neq 0$ also give a small but positive eLE, as shown in Fig. 9. While diverged trajectories may appear in presence of a positive eLE (Fig. 9a), the system is conservative because the summation of the three LEs is zero (Fig. 9d). In comparison between the first LEs of the ensemble runs from the 3D-NLM with $r = 0$ and $r = 5$, the first LEs with $r = 5$ are larger, which may indicate the role of the heating term in destabilizing the solutions. Note that X-Y section of the solutions with $r = 5$ display a comparable pattern to that of the solution in Fig 5 where $r = 25$.

The impact of different ICs (i.e., X_o in Fig. 7) on the calculation of eLE is briefly discussed with the following analysis of the critical points in the X-Y section. As discussed in Fig. 5a, a solution may move "around" the saddle point and the two stable critical points, and its trajectory defines the big cycle. With a different initial condition, a solution may go around one of the non-trivial stable points ($\pm\sqrt{2\sigma r + X_0^2}$, 0) and its trajectory forms a small cycle. For example, Fig. 5d, displays results with three different ICs, including X_0 = $\sqrt{2\sigma r}$, $\sqrt{2\sigma r}$ + 15 and $\sqrt{2\sigma r}$ + 30 in black, blue and red lines, respectively. Three vertical green lines show the locations of the corresponding stable critical

points at $X_c = \sqrt{2\sigma r + X_0^2}$. Solutions in Figures 5a and 5d suggest that the larger initial X_o is, the further the trajectory is away from the saddle point. Thus, the ensemble LE obtained with different ICs represents the average stability of solutions, some of which may have trajectories similar to that in Fig. 5d (under small or no significant influence of the saddle point), and the others are close to those in Fig. 5a (under the influence of the saddle point). For the former, with an initial condition away from the saddle point, the nonlinearity may become dominant, as compared to the (linear) heating term. The corresponding solutions (e.g., the blue curve in Fig. 5d) become more symmetric with respect to the green line that passes through the nontrivial stable critical point. For the latter, two trajectories that move toward the saddle point may experience different growth rates. They may form a big or small cycle.

Numerical solutions of the 3D-NLM with $r = 0$ are analyzed to study the role of nonlinearity (i.e., nonlinear feedback loop) in producing diverged trajectories, leading to a small but positive eLE (over a long but finite time period). Using the initial conditions (ICs) of $(X, Y, Z) = (0, Y_{ic}, 0)$, we consider the control run with $Y_{ic} = 1$ and the parallel run with $Y_{ic} = 1 + \epsilon$, here ϵ indicates an initial perturbation. Therefore, Eq. (21) is generalized as:

$$Y^2 + \left(\frac{X^2}{2\sigma}\right)^2 = Y_{ic}^2, \tag{1}$$

which has the following solutions:

$$Y = Y_{ic}\cos(\phi), \tag{2a}$$

$$\phi = \int\int Y \,\mathrm{d}\tau_1\tau_2. \tag{2b}$$

Y_{ic} and ϕ represent the amplitude and phase of the solution, respectively. For both of the control and parallel runs, the solution in Eq. 27a suggests that the amplitude of the solution remains unchanged during the entire period. While the instantaneous value of the solution at a given time step is determined by its phase (e.g., Eq. 27a), the phase is a function of the instantaneous value of the solution at the previous time step (e.g., Eq. 27b). The mutual dependence between the instantaneous value and phase, which is a result of the nonlinearity, may lead to the divergence of two trajectories (over a long but finite-time period) between the control and parallel runs, illustrated below.

In general, the time change of the phase ($d\phi/d\tau = X$ in Eq. 23a) is not a constant but is a function of the solution's value. When ϵ is tiny, the amplitudes of the solutions for the control and parallel runs are very close. However, as a result of the nonlinear characteristic (as shown with Eqs. 27a-b), the tiny difference in the initial conditions for the two runs may lead to significant differences in their phases. Figure 10 show the time evolution of the numerical solutions from the 3D-NLM with $r = 0$ for the control and parallel runs (with $\epsilon = 0.001$) and their differences. A very large time period of $\tau = 6000$ is used. The shift of the phases between the two runs is clearly shown in Figs. 10a-10b, while the amplitudes of both solutions (i.e., maxima) remain unchanged during the integration. As a result of the phase shift, the differences between the two solutions appear, growing initially and

then decaying. The former leads to the divergence of two trajectories over a finite-time period (e.g, Figs. 10c-d). The differences of two runs are oscillatory and have a period showing dependence on solutions (Y or Z) and initial conditions. The long period (e.g., $\sim 4,600$ in Fig. 10c and $\sim$ 2,300 in Fig. 10d), which cannot be determined in advance, makes it challenging to choose a total integration time (or a sampling time interval) for the calculations of an global (or finite-time) eLE that can accurately describe the global (local) stability of the 3D NLM. Therefore, although a fixed total time of τ=1000 is sufficiently large to obtain the eLE in the original Lorenz model (e.g., Shen 2014a), it is still too short for the conservative 3D NLM. This may suggest that with no prior knowledge of the period which may depend on the the fields and initial conditions, it is challenging to apply the current method to calculate the eLE in a conservative system such as he 3D NLM.

This phenomenon, which is associated with the dependence of phases on the amplitude, may be simply illustrated in Fig. 11 by observing the the different "phase" speeds of short and long hands of "clock," which conceptually represent the solutions of the control and parallel runs, respectively. Initially, both hands are at the same position (i.e., the same phase in dashed lines with arrows in Fig. 11), but gradually depart as a result of different moving speeds (in solid lines with arrows in Fig. 11). Note that the moving speed for each hand of the clock is a constant but not a function of time, which is fundamentally different from the (nonlinear) solutions of the 3D-NLM.

In a brief summary, for trajectories near a stable critical point, e.g., $(X, Y) = (0, 0)$ for $r = 0$ or $(X, Y) = (\sqrt{2\sigma r + X_0^2}, 0)$ for $r \neq 0$ and a large X_o, the nonlinearity may act as a forcing term in producing diverged trajectories, because nonlinearity alone may continuously change the phase of the solution. When the heating term becomes important to change the amplitude of the solution, its interaction with the nonlinearity can also lead to diverged trajectories.

Acknowledgements. We thank Prof. Zdzislaw Musielak, Dr. Tzi-Cheng Lai, Profs. Xubin Zeng, Ricardo Carretero, and Juan Serna, and one anonymous reviewer for valuable comments and/or discussions, and Jill Dunbar for proofreading this manuscript. We are grateful for support from the NASA Advanced Information System Technology (AIST) program of the Earth Science Technology Office (ESTO) and from the NASA Computational Modeling Algorithms and Cyberinfrastructure (CMAC) program. Resources supporting this work were provided by the NASA High-End Computing (HEC) Program through the NASA Advanced Supercomputing (NAS) Division at Ames Research Center.

Appendix A: Derivations of Eq. (3)

In this section, we describe the procedures to derive Eq. (3). As discussed in Shen (2014a), the nonlinear advection term in Eq. (1) does not appear explicitly in the Lorenz model. Therefore, Eq. (1) can be written as follows:

$$\frac{\partial}{\partial t}\nabla^2\psi = g\alpha\frac{\partial\theta}{\partial x}. \qquad (A1)$$

With the $M_1 - M_3$ of Shen (2014a), ψ and θ can be represented as

$$\psi = C_1 X M_1, \tag{A2}$$

$$\theta = C_2 \left(Y M_2 - Z M_3 \right). \tag{A3}$$

Here, C_1 and C_2 are defined in Eq. (9) of Shen (2014a). Next, we express the left- and right-hand side terms of Eq. A1 using $M_1 - M_3$, respectively, as follows:

$$\frac{\partial}{\partial t} \nabla^2 \psi = -C_1 \left(l^2 + m^2 \right) \frac{dX}{dt} M_1, \tag{A4}$$

$$g\alpha \frac{\partial \theta}{\partial x} = C_2 Y g\alpha (-\sqrt{2}) l sin(lx) sin(mz) = -C_2 Y g\alpha l M_1. \tag{A5}$$

Here l and m, defined in Shen (2014a), represent the horizontal and vertical wavenumbers, respectively. Substituting Eqs. A4 and A5 into Eq. A1, we have:

$$\frac{dX}{dt} = \frac{g\alpha l}{l^2 + m^2} \frac{C_2}{C_1} Y. \tag{A6}$$

We define a time scale (T_o) as

$$T_o = (1 + a^2) \frac{\pi^2}{H^2}, \tag{A7}$$

and obtain

$$l^2 + m^2 = (1 + a^2) \frac{\pi^2}{H^2} = T_o. \tag{A8}$$

Here, the term H is the domain height, and a is a ratio of the vertical scale of the convection cell to its horizontal scale, (i.e., $a = l/m$). With Eq (9) in Shen (2014a), the right-hand side of Eq. A6 becomes

$$\frac{g\alpha l}{l^2 + m^2} \frac{C_2}{C_1} Y = \frac{H^2}{\pi^2 (1 + a^2)} \frac{g\alpha \pi a}{H} \frac{a}{\kappa (1 + a^2)} \frac{\Delta T}{\pi} \frac{R_c}{R_a} Y = \nu (1 + a^2) \frac{\pi^2}{H^2} = \nu T_o Y. \tag{A9}$$

With Eq. A9, Eq. A6 becomes

$$\frac{dX}{dt} = \nu T_o Y. \tag{A10}$$

The above equation turns into Eq. (3), $dX/d\tau = \sigma Y$, when $\tau = \kappa T_o t$ is assumed.

Appendix B: A closed-form solution using elliptic functions

Nonlinear dynamics have been widely studied using the solutions to the nonlinear Duffing equation. The Duffing equation that governs certain damped and driven (i.e., dissipative and forced) oscillatory motions (Bender and Orszag, 1978; Wikipedia) is given by

$$\frac{d^2 X}{d\tau^2} + \delta \frac{dX}{d\tau} + \alpha X + \beta X^3 = \gamma cos(\omega \tau), \tag{B1}$$

here δ, α, β, γ, and ω are constants. When $\delta = \gamma = 0$ and $\alpha = -\sigma r$ and $\beta = 1/2$, Eq. B1 appears in the form of the 3D-NLM (Eq. 15). While an exact solution to the general form of the

Duffing equation may not been found, closed-form, approximated or numerical solutions have been documented in the literature. In this section, we discuss how a closed-form solutions to the special
130 case of the non-dissipative and unforced Duffing equation (i.e., $\delta = \alpha = \gamma = 0$ and $\beta = 1/2$) can be obtained and expressed in terms of elliptic functions (Davis, 1960).

The incomplete elliptic integral of the first kind, $F(\phi, k)$, is written as

$$u = F(\phi, k) = \int_0^{\phi} \frac{d\theta}{\sqrt{1 - k^2 sin^2\theta}}. \qquad 0 < k^2 < 1. \tag{B2}$$

The elliptic functions of Jacobi are defined as inverse of the elliptic integral as follows:

$$sn(u, k) = sin\phi, \qquad cn(u, k) = cos\phi. \tag{B3}$$

The elliptic functions have the following properties

$$sn(0) = 0, \qquad cn(0) = 1, \qquad sn^2 u + cn^2 = 1, \tag{B4}$$

and their derivatives can be obtained as follows:

$$\frac{d^2}{du^2} sn(u) = 2k^2 sn^3(u) - (1 + k^2) sn(u), \tag{B5}$$

and

$$\frac{d^2}{du^2} cn(u) = (2k^2 - 1) cn(u) - 2k^2 cn^3(u). \tag{B6}$$

Equations B4 and B5 can help obtain the solution to the equation $d^2X/d\tau^2 + X^3/2 = 0$ (i.e., Eq. 18). With Eq. B5 and $k^2 = -1$, the solution can be written as

$$X = D_1 sn(\frac{D_1}{2}\tau + \theta_1, k^2 = -1). \tag{B7}$$

With Eq. B6 and $k^2 = 1/2$, the solution becomes

$$X = D_2 cn(\frac{D_2}{\sqrt{2}}\tau + \theta_2, k^2 = 1/2). \tag{B8}$$

Here, D_1, D_2, θ_1 or θ_2 are constants and determined by the initial conditions. θ_1 or θ_2 can be expressed in terms of the complete elliptic integrals of the first kind $K(k) = F(\pi/2, k^2 = 1/2) \sim 1.8541$, which is calculated with Matlab (http://www.mathworks.com/help/matlab/ref/ellipke.html). In addition, as a result of the definition of the elliptic integral (e.g., Eq. B2) and/or the validity of the numerical algorithms for the elliptic functions, k^2 may not be equal to -1. Therefore, only Eq. B8 is discussed below. In this study, the IC with $X(0) = 0$ and $Y(0) = 1$ (i.e., $\frac{d}{d\tau}X(0) = \sigma$)) leads to the following solution with $\theta_2 = 3K$ and $D_2 = \sqrt{2\sigma}$:

$$X = \sqrt{2\sigma} cn(\sqrt{\sigma}\tau + 3K, k^2 = 1/2). \tag{B9}$$

Figure B1 displays the solutions from Eqs. 22a (Fig. B1-a) and Eq. B9 (Fig. B1-b) and their differences (Fig. B1-d), showing very close results. This comparison confirms the validity of

the method for obtaining the closed-form solutions to the 3D-NLM with $r = 0$ using elementary trigonometric functions (Fig. 2), which are used to illustrate the impact of nonlinearity on the changes of the solution's phase in section 3.4. For the case with $\alpha \neq 0$ (i.e., $r \neq 0$), similar procedures can be applied using Eq. B5 or B6 to obtain closed-form solutions, which is beyond the scope of this study.

References

Bender, C. M. and Orszag, S. A.: Advanced Mathematical Methods for Scientists and Engineers, McGraw-Hill, New York, 593 pp., 1978.

Christiansen, F., and H. Rugh, 1997: Computing Lyapunov Spectra with Continuous Gram-Schmid Orthonormalization. *Nonlinearity* 10, 1063-1072.

Davis, H. T., 1960: Introduction to Nonlinear Differential and Integral Equations. U.S. Atomic Energy Commission, September, 1960. 566pp.

Ding, R. O., and J. P. Li, 2007: Nonlinear finite-time Lyapunov exponent and predictability. *Phys. Lett.*, **354A**, 396-400.

Eckhardt, B. and D. Yao, 1993. Local Lyapunov exponents in chaotic systems. *Physica D*, **65**, 100-108.

Froyland, J. and K. H. Alfsen, 1984: Lyapunov-exponent spectra for the Lorenz model.

Kazantsev, E., 1999: Local Lyapunov exponents of the quasi-geostrophic ocean dynamics, *Applied Mathematics and Computation*, **104**, 217-257.

Li, J. and R. Ding, 2011: Temporal-Spatial Distribution of Atmospheric Predictability Limit by Local Dynamical Analogs. *Mon. Wea. Rev.*, **139**, 3265-3283.

Nese, J. M., 1989: Quantifying local predictability in phase space. *Physica*. **35D**, 237-250.

Sprott, J. C., 2003: *Chaos and Time-Series Analysis.* Oxford University Press. 528pp. The numerical method is briefly discussed on http://sprott.physics.wisc.edu/chaos/lyapexp.htm.

Thiffeault, J.-L. and Horton, W.: Energy-conserving truncations for convection with shear flow, Phys. Fluids, 8, 1715–1719, 1996.

Wolf, A., J. B. Swift, H. L. Swinney, and J. A. Vastano, 1985: Determining Lyapunov Exponents from a Time Series. *Physica*, **16D**, 285-317.

Zeng, X., R. Eykholt, and R.A. Pielke, 1991: Estimating the Lyapunov-exponent spectrum from short time series of low precision. *Phys. Rev. Lett.*, **66**, 3229-3232.

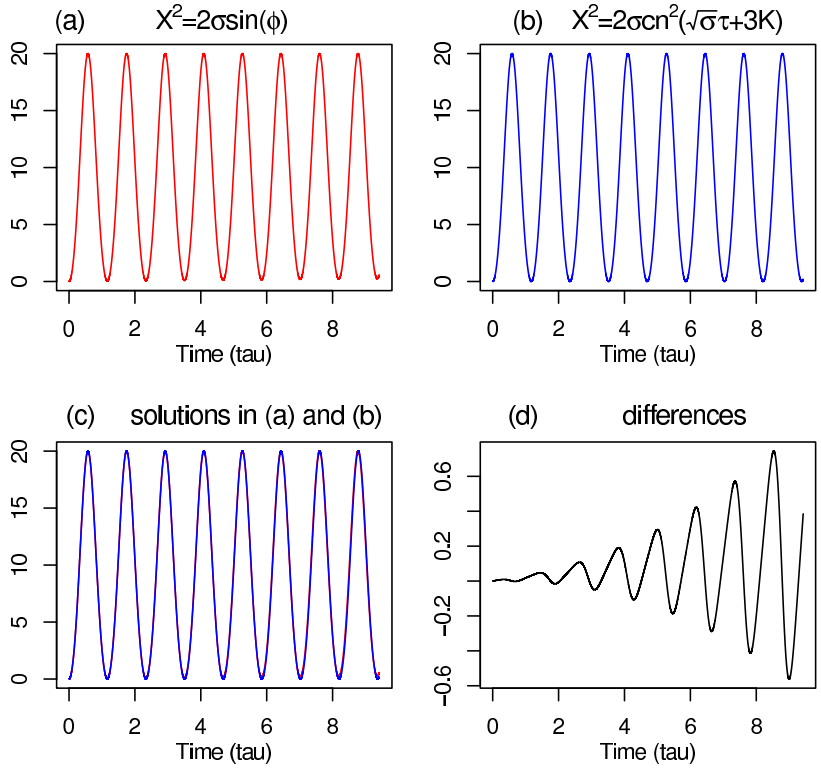

Figure B1: A comparison of the solutions in Eqs. (22a) and (B9), which are expressed using an elementary trigonometric function and an elliptic function, respectively. (a) the solution of Eq. (22a) in red. (b) the solution of Eq. (B9) in blue. (c) both of the solutions in (a) and (b). (d) differences of the two solutions.

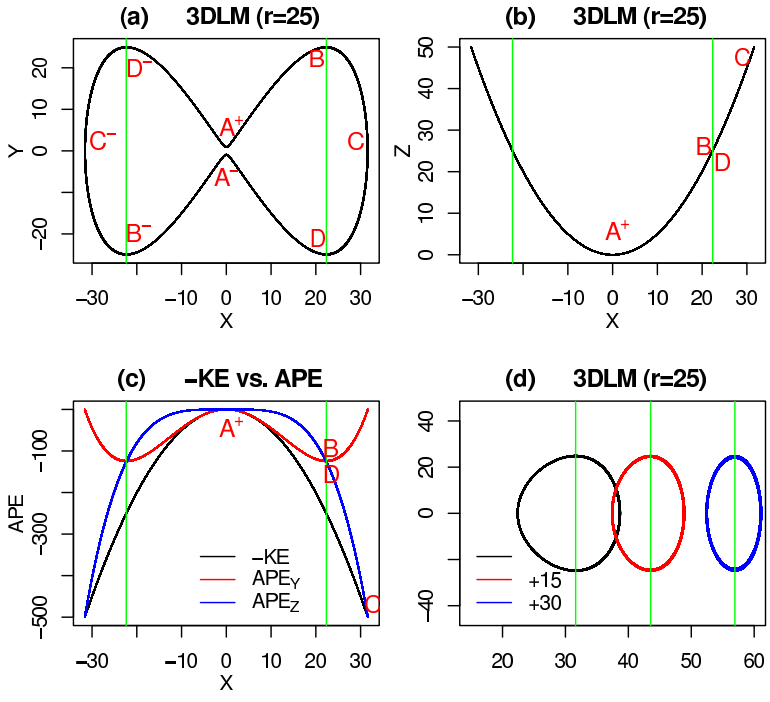

Figure 5. Solutions from the 3D-NLM (Eqs. 3–5). **(a)** X–Y plot. **(b)** X–Z plot. **(c)** X-APE plot. The black, red, and blue lines show normalized $-$KE, APE$_Y$ and APE$_Z$, respectively. Green lines are plotted at $X = \pm X_{\rm t} = \pm\sqrt{2\sigma r}$ where $Y^2 = Z^2$. (d) X-Y plot with different initial conditions, $(X, Y, Z) = (X_0, 0, 0)$. The black, red and blue curves represent results with X_0 = $\sqrt{2\sigma r}$, $\sqrt{2\sigma r}$ +15 and $\sqrt{2\sigma r}$ + 30, respectively. Three green lines pass through the corresponding critical points at (X_c, Y_c) = ($\sqrt{2\sigma r + X_0^2}$, 0).

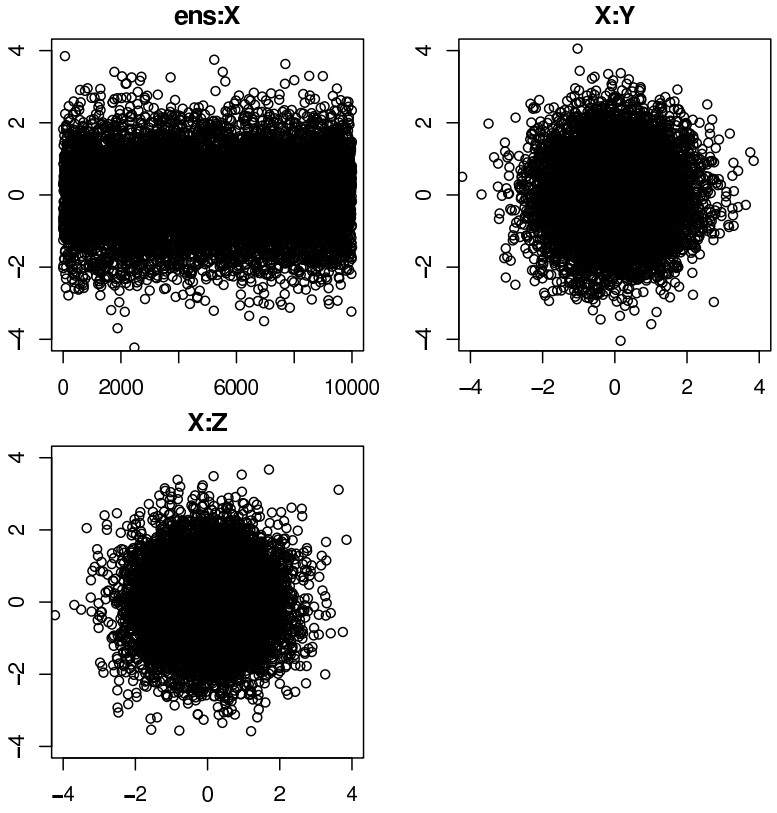

Figure 7. 10,000 initial conditions for the calculation of the ensemble Lyapunov exponent. (a) The distribution of X as a function of the ensemble members. (b) The distributions of X and Y. (c) The distributions of X and Z.

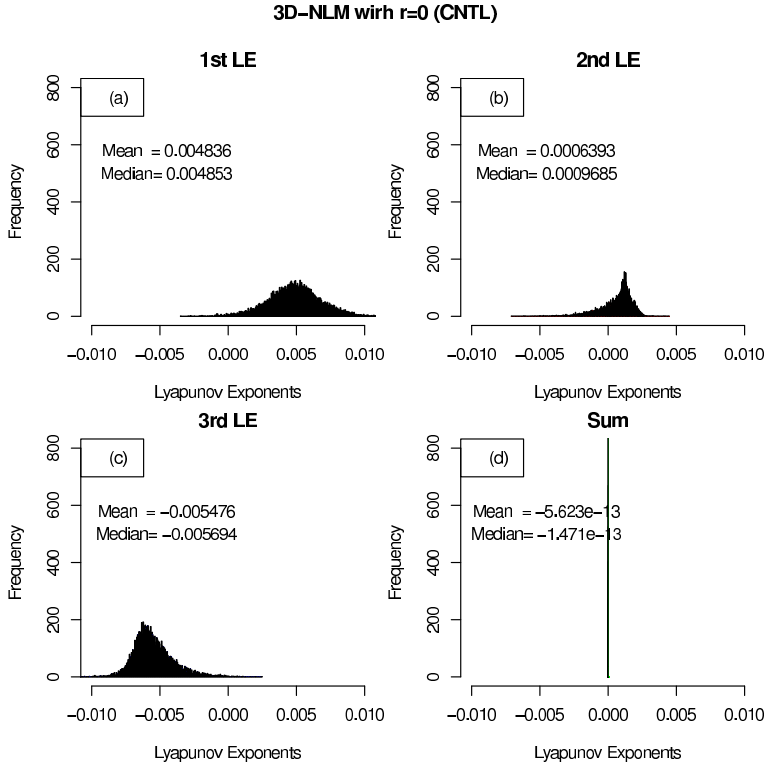

Figure 8. The Lyapunov exponents and their summation for the 3D-NLM with $r = 0$. Panels a-c show the histograms of the first, second, and third LEs from the ensemble runs, respectively. (d) Summation of the three LEs.

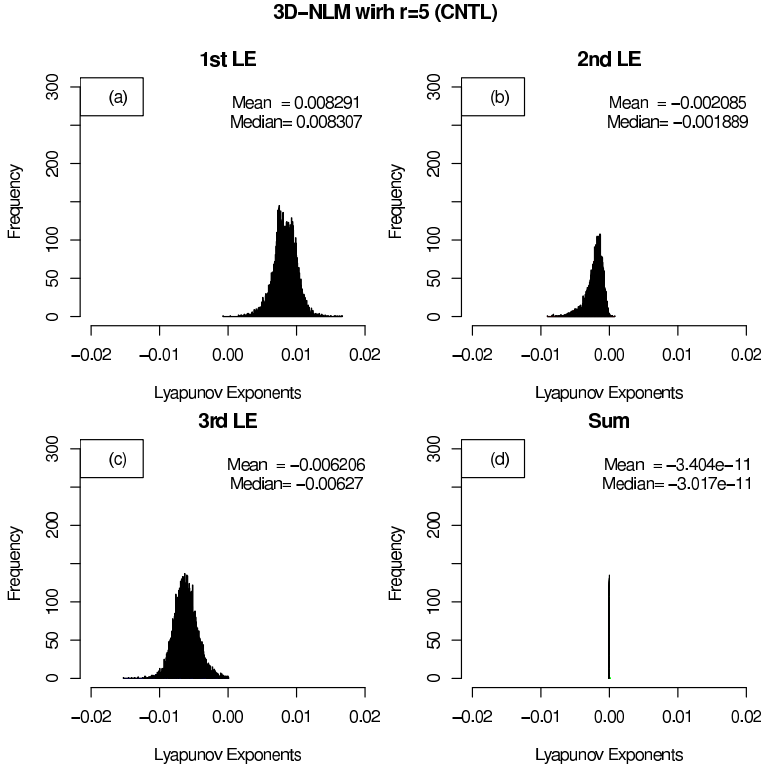

Figure 9. As in Figure 8, but for $r = 5$.

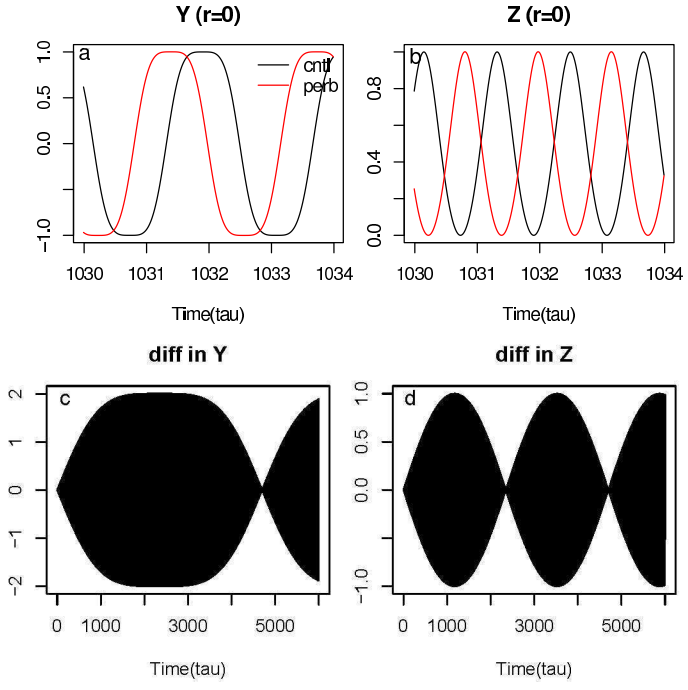

Figure 10. Time evolution of numerical results for the control run (black) and parallel run (red) using the 3D-NLM with $r = 0$. A tiny initial perturbation ($\epsilon = 0.001$) is used. (a) Y plot. (b) Z plot. (c-d) Differences of Y and Z between the control and parallel runs.

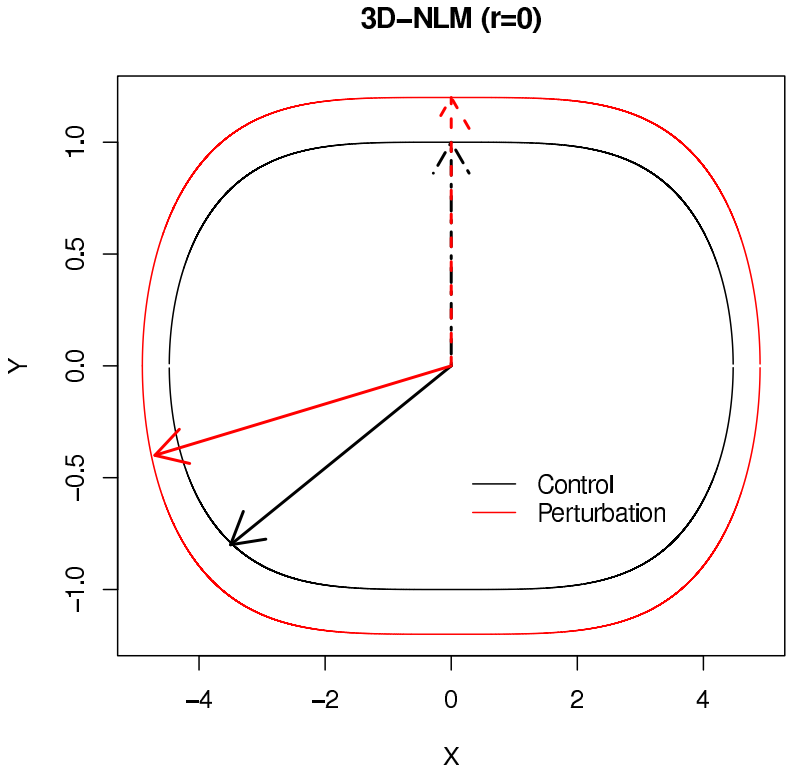

Figure 11. A X-Y plot for the control run (black) and parallel run (red). The initial conditions, $(X, Y, Z) = (0, Y_{ic}, 0)$, include $Y_{ic} = 1$ for the control run and $Y_{ic} = 1 + \epsilon$ for the parallel run. A large ϵ $(= 0.2)$ is used for better illustration. [In Fig. 10, $\epsilon = 0.001$ is used.] At a given time, the position in each of the trajectories is indicated by the location of an arrow. As a result of the nonlinearity and the initial perturbation, the arrows of the two runs move at different speeds, leading to the divergence of two trajectories.